

# Photoinduced Isomerization Kinetics of Diiodomethane in Supercritical Fluid Solution: Local Density Effects<sup>†</sup>

Christian Grimm,<sup>‡</sup> Alexander Kandratsenka,<sup>§</sup> Philipp Wagener,<sup>‡</sup> Jochen Zerbs,<sup>‡</sup> and Jörg Schroeder<sup>\*,‡,§</sup>

*Institut für Physikalische Chemie, Universität Göttingen, Tammannstrasse 6, 37077 Göttingen, Germany, and Max-Planck-Institut für Biophysikalische Chemie, Am Fassberg, 37077 Göttingen, Germany*

*Received: October 1, 2005; In Final Form: December 9, 2005*

The density dependence of diiodomethane photoinduced isomerization in supercritical (sc) CO<sub>2</sub>, CHF<sub>3</sub>, and C<sub>2</sub>H<sub>6</sub> was investigated by transient absorption spectroscopy, covering a fluid density range from 0.7 to 2.5 (in reduced units). The solvent-caged photoproduct iso-diiodomethane is formed even at the lowest density, and its yield increases about 4-fold over the whole range. At the same time, isomer formation rate constants increase by roughly an order of magnitude and show little variation between CO<sub>2</sub>, C<sub>2</sub>H<sub>6</sub>, and CHF<sub>3</sub>. Furthermore, the formation rate constant decreases significantly with increasing excitation energy. We propose an isomer formation mechanism involving a rapidly established preequilibrium between a solvent-caged iodine atom–methyl iodide radical pair and a loosely bound iodine–methyl iodide radical complex, from which the reaction subsequently proceeds to the isomer. The latter step seems to be controlled by collisional stabilization of the initially hot radical moiety, as the formation rate constant increases linearly with sc solvent viscosity. The model predicts a quadratic dependence of relative isomer yield on fluid density. A corresponding correlation is found with the local fluid density, calculated via solute–solvent radial distribution functions obtained from molecular dynamics (MD) simulations.

## 1. Introduction

The “photolytic cage effect” proposed by Franck and Rabinovitch in the mid 1930s,<sup>1</sup> the result of competition between escape from a solvent cage and an in-cage reaction of a photolytically generated reactant pair, belongs intuitively to the most obvious effects of a dense fluid environment on chemical reactions. It was first studied systematically by Noyes and co-workers<sup>2–5</sup> who observed the reduction of the iodine photodissociation quantum yield  $\Phi_d$  from unity in the gas phase to around 0.4 in liquid solution. Exploiting the advantages of supercritical (sc) solvents, Luther and Troe investigated the pressure dependence of  $\Phi_d$ <sup>6</sup> and found that it decreases already at densities significantly below those typical of liquid solution. Further studies in this direction (see ref 7 for a review) led to a refinement of Noyes’ original diffusion model of the iodine photolytic cage effect. In particular, the dependence of vibrational energy relaxation (VER) of iodine molecules on sc solvent density was taken into account explicitly,<sup>7</sup> in view of the crucial role of VER in stabilizing iodine molecules formed by in-cage atom combination.<sup>1,8</sup>

Following the pioneering picosecond experiment by Eisenthal and co-workers, a deeper understanding of the cage dynamics was obtained from time-resolved experiments carried out by a number of groups during the 1980s and 1990s.<sup>9–12</sup> (See ref 13 for a review of earlier work.) In addition to VER on the ground-state potential, trapping in weakly bound electronically excited states followed by radiative or nonradiative return to the ground

state as well as direct cage escape were found to be of significance. These findings were corroborated by classical<sup>13–17</sup> and mixed quantum-classical<sup>18–20</sup> MD simulations which suggested that branching between escape and recombination occurs early within the first few picoseconds after excitation, ruling out diffusive motion as the controlling process. In recent experimental reinvestigations of the density dependence of  $\Phi_d$  accompanied by classical MD simulations,<sup>21,22</sup> it was found that for solvents as diverse as sc xenon and compressed liquid *n*-heptane  $\Phi_d$  correlates with the reduced density  $\rho_r = \rho/\rho_c$  of the solvent ( $\rho$  and  $\rho_c$  are the density and the critical density of the solvent, respectively) over the entire density range from gas to liquidlike, confirming an earlier suggestion by Bunker that caging is controlled by the packing density of surrounding solvent molecules rather than by solvent friction.<sup>13</sup>

Because of the practical importance the cage effect has in radical pair chemistry,<sup>23</sup> it would be desirable to perform similarly detailed studies on polyatomic molecules. In this case, in-cage dynamics might be affected by internal energy of radical fragments, intramolecular multidimensional dynamics, or possibly competition between different in-cage reactions, vibrational relaxation, and cage escape. Recently, we reported on first steps in this direction by looking at the photochemical kinetics of diiodomethane (CH<sub>2</sub>I<sub>2</sub>) in sc fluid solution.<sup>24,25</sup> This molecule is a promising candidate, because its photodissociation is sufficiently rapid not to be quenched to any large extent in liquid solution<sup>24,26–31</sup> and a fast in-cage reaction product was observed by femtosecond transient absorption spectroscopy which could be identified as iso-diiodomethane (CH<sub>2</sub>I–I).<sup>28</sup> This assignment was confirmed by a combination of time-resolved resonance Raman measurements with quantum-chemical density functional

<sup>†</sup> Part of the special issue “Jürgen Troe Festschrift”.

<sup>\*</sup> To whom correspondence should be addressed. E-mail: jschroe2@wdg.de.

<sup>‡</sup> Universität Göttingen.

<sup>§</sup> Max-Planck-Institut für Biophysikalische Chemie.

theory (DFT) calculations<sup>32–34</sup> and recent picosecond time-resolved X-ray diffraction measurements in methanol solution.<sup>35</sup>

In the gas phase, irradiation of diiodomethane in the UV region around 300 nm is well-known to cause C–I bond dissociation to form a  $\text{CH}_2\text{I}$  radical and a ground- or excited-state iodine atom<sup>36–40</sup> on a time scale a lot shorter than the molecular rotational period,<sup>36,41</sup> which is about 6.5 ps (estimated from  $\text{CH}_2\text{I}_2$  rotational constants).<sup>42</sup> About 80% of the available energy after photolysis at 304 nm appears as internal energy of the nascent radical,<sup>40,41</sup> which is highly excited close to the vibrational quasi-continuum.<sup>37</sup> For excitation into the lowest energy absorption band, this has been rationalized in terms of a dynamical two-dimensional (2D) model,<sup>43</sup> in which Franck–Condon excitation is along the I–C–I symmetric stretch and subsequent dissociation takes place predominantly on the repulsive excited-state surface along the antisymmetric I–C–I-stretch. Close to the dissociation limit the two modes will be strongly coupled, such that it takes on the order of 100 fs to complete the process. In corresponding 3D wave packet model calculations using the same empirical potential direct dissociation turns out to be even faster.<sup>44</sup> To what extent such models represent  $\text{CH}_2\text{I}_2$  photodissociation dynamics remains to be clarified by future calculations on more realistic *ab initio* potential energy surfaces.

In liquid solution, the details of  $\text{CH}_2\text{I}_2$  photodissociation dynamics have been a subject of debate. The interpretation and assignment of transient absorbance signals obtained from femtosecond pump–probe spectroscopy varied considerably, although the basic experimental result presented by three different groups is practically identical.<sup>26–28</sup> The transient absorbance signals observed after UV-excitation consist of three main components, a fast rise apparently limited by the cross correlation of pump and probe pulses, a subsequent fast decay on a time scale of 200–300 fs followed by a slower absorbance increase with a rise time of several picoseconds until the signal reaches a plateau which persists on a nanosecond time scale. The acceleration of the slow rise with increasing  $\text{CH}_2\text{I}_2$  concentration reported by Saitow et al.<sup>27</sup> however could not be verified in later work.<sup>28,30</sup>

Tarnovsky, Åkesson, and co-workers<sup>28–30</sup> presented a detailed study on  $\text{CH}_2\text{I}_2$  photodissociation in acetonitrile solution on the basis of measurements with 310 nm excitation and broadband detection from 290 to 1220 nm. They critically reassessed the assignment of the absorption transients that had been observed before.<sup>26,27</sup> They compared the observed transient absorption bands at 390 and 570 nm with spectra from a  $\text{CH}_2\text{I}_2$  matrix photochemistry by Maier et al.<sup>45</sup> who had attributed these bands to the  $\text{CH}_2\text{I}$ –I isomer. On the basis of this assignment and an analysis of the observed time evolution of their transient spectra, they concluded that (i) the fast, initial 350 fs decay monitors the outgoing wave packet on the repulsive excited-state potential energy surface of  $\text{CH}_2\text{I}_2$ , (ii) a vibrationally hot  $\text{CH}_2\text{I}$ –I isomer is already formed within the first picosecond and subsequently relaxes within about 10 ps, causing the slowly rising component, and (iii) the radical fragment is observed at short probe wavelengths  $\leq 380$  nm only, where its absorption appears within 0.3 ps and decays within about 3 ps. This implies that the dynamics are described as a sequential two-step process involving rapid (350 fs) dissociation into a  $\text{CH}_2\text{I}$  radical–iodine atom pair in the solvent cage and subsequent almost equally fast ( $\sim 1$  ps) recombination to form the isomer, at most requiring a couple of collisions with molecules of the solvent-cage wall. As most of the available energy in the dissociation is deposited as internal energy of the radical and both steps are fast compared

to vibrational relaxation times, the radical and isomer initially are highly vibrationally excited and by energy transfer to the solvent cool on picosecond time scales maintaining quasi-equilibrium between the isomer and caged radical atom pair. The isomerization quantum yield in liquid solution seems to be fairly high: for 266/350 nm excitation, values of  $\sim 0.7$  and  $\sim 0.5$  were estimated for diiodomethane and iodoform in acetonitrile, respectively.<sup>29,30</sup>

This description is in agreement with conclusions concerning the isomer product derived from independent transient resonance Raman spectroscopy following photodissociation of diiodomethane in solution, in which the  $\text{CH}_2\text{I}$ –I isomer also was identified as the species responsible for the two transient absorption bands at 390 and 570 nm.<sup>32–34</sup> The assignment was based on a comparison of transient Raman bands observed in pico- and nanosecond experiments with IR spectra from the matrix isolation work by Maier et al.<sup>45</sup> and normal-mode frequencies derived from DFT calculations. Furthermore, the temporal evolution of the Stokes Raman spectra exhibits a slight blue shift and increase of band intensity indicative of a vibrational cooling process. From their data, Phillips and co-workers concluded that the “hot” isomer is formed within a few picoseconds and that subsequent vibrational relaxation takes place on a time scale of tens of picoseconds.<sup>33</sup> A similar photodissociation/isomerization mechanism in solution was also proposed for other polyhalomethanes such as  $\text{CH}_2\text{ClI}$ ,  $\text{CH}_2\text{BrI}$ , and  $\text{CHI}_3$  based on femtosecond transient absorption experiments<sup>29,46,47</sup> and resonance Raman studies.<sup>48–51</sup>

It is still an open question, however, how the direct dissociation in the gas phase turns into isomerization as the solvent cage gradually builds up. Studies in sc solution are well suited to address this point and to further clarify the isomerization mechanisms, as solvent-cage properties may be tuned continuously by varying the fluid density from gas to liquidlike. Recently, we reported on first experiments in sc  $\text{CO}_2$ ,  $\text{C}_2\text{H}_6$ , and  $\text{CHF}_3$ ,<sup>24,25</sup> which showed the expected increase of the isomerization quantum yield with density. We also observed a decrease of the isomer absorption rise time with increasing density, consistent with the proposition that vibrational cooling is a controlling step in isomer formation. As far as the central aspects of the mechanism are concerned—build-up of isomer from some form of caged pair and subsequent and concurrent vibrational cooling—our results supported the conclusions drawn from liquid-phase studies.<sup>28,30</sup> However, the reduced density range we covered in these experiments was restricted to  $1.5 < \rho_r \leq 2.4$ , not extending to values sufficiently close to the gaslike regime. We also observed an almost exponential increase of the isomer formation rate constant with density, which is stronger than the linear dependence of VET rates on local density observed in sc solution.<sup>52,53</sup>

In the work reported here, we concentrate on the density effect on isomer formation kinetics, that is, on rate constants and yields, covering an extended density range in sc  $\text{CO}_2$ ,  $\text{C}_2\text{H}_6$ , and  $\text{CHF}_3$ . We also briefly consider the variation of the initial internal energy by changing the excitation wavelength. On the basis of these results, we propose a simple kinetic model in an attempt to rationalize the experimental results and to address the points raised above.

## 2. Experimental Technique

Details of the pump–probe setup have been described elsewhere.<sup>24</sup> In brief, we used a 1 kHz Ti:Sapphire regenerative amplifier (Clark-MXR CPA2001) as the femtosecond light source delivering pulses of 0.9 mJ energy and 150 fs duration

at 773 nm which were used to pump two commercial optical parametric amplifiers, a Yobin Yvon two stage NOPA ( $1/3$  of pump intensity) and a Light Conversion TOPAS ( $2/3$  of pump intensity). After frequency doubling, these provided tunable pump and probe pulses, respectively. The spectral width of the pump pulses at 304 nm was measured to be about 7 nm (assuming Gaussian band shape), corresponding to a pulse duration of  $\sim 140$  fs; their energy was approximately  $0.5 \mu\text{J}$ . Probe pulses were taken directly from the computer-controlled TOPAS using its internal nonlinear mixing and wavelength separation facilities. Their spectral width was about 5 nm throughout the spectral range studied in our experiments. The temporal half-width of the pump–probe cross correlation was typically between  $120 \pm 5$  fs (304 nm pump/405 nm probe) and  $200 \pm 15$  fs (304 nm pump/370 nm probe). We used a conventional pump–probe arrangement employing an optical delay line with nominal 0.7 fs step size. Incident and transmitted probe pulse energies were measured by integrating photodiodes (Hamamatsu 1226-8BQ or 1336-8BQ0A). Pump and probe beams were focused into the sample cell by parabolic mirrors to beam waist diameters of approximately 300 and 150  $\mu\text{m}$ , respectively. Relative polarization of pump and probe beams was controlled by a tunable zero-order half-wave plate. Experiments were performed under magic angle conditions. Transient absorbance traces were taken by recording incident to transmitted probe pulse energy ratios alternating between pump pulse on and off, that is, in synchronization with a chopper positioned in the pump pulse beam. At each delay position, 200–1000 measurements were averaged and every final trace was the result of 6–8 scans over the whole time range.

The basic design of the stainless steel 100 MPa high-pressure sample cell was developed in Prof. O. Kajimoto's group at Kyoto University. It contains a small sample reservoir and a magnetic stirrer, and its effective optical length between sapphire windows of 2 mm thickness is 2.5 mm. In the present design, using Teflon O-rings and silicon varnish for sealing the windows, the cell may be heated to about 50  $^{\circ}\text{C}$  using temperature control ensuring  $\pm 0.5$   $^{\circ}\text{C}$  stability. It was connected to a high-pressure system via line filters to prevent contamination with residual oxygen or water. For transient absorption measurements, the sample reservoir was filled with a defined amount (typically about  $2 \mu\text{L}$ ) of liquid diiodomethane before the cell was pressurized with sc fluid. Around 10 MPa pressure, diiodomethane dissolved quantitatively forming a homogeneous mixture, resulting in a diiodomethane concentration of  $\sim 10^{-2}$  mol/L and a sample absorbance at the pump wavelength of about 2.5, such that more than 99% of the pump light was absorbed.

Diiodomethane (Merck-Schuchardt, for synthesis, >99%),  $\text{CHF}_3$ ,  $\text{CO}_2$  (Messer-Griesheim, grade 4.5), and  $\text{C}_2\text{H}_6$  (Messer-Griesheim, grade 2.5) were used as supplied without further purification.

### 3. Simulations

Local sc  $\text{CO}_2$  solvent densities in the vicinity of the solute were calculated on the basis of solute–solvent center-of-mass radial distribution functions  $g(r)$  obtained from classical MD simulations performed with the MOLDY<sup>54</sup> package. The simulation box contained 200 solvent molecules and a single diiodomethane solute molecule. The number of solvent molecules was found to be sufficient for the purpose of calculating  $g(r)$  to the required accuracy. After an initial equilibration period of 200 ps, trajectories of 2 ns duration were simulated with a step size of 2 fs.

The following intermolecular potentials of the pure substances were used as described in the literature:

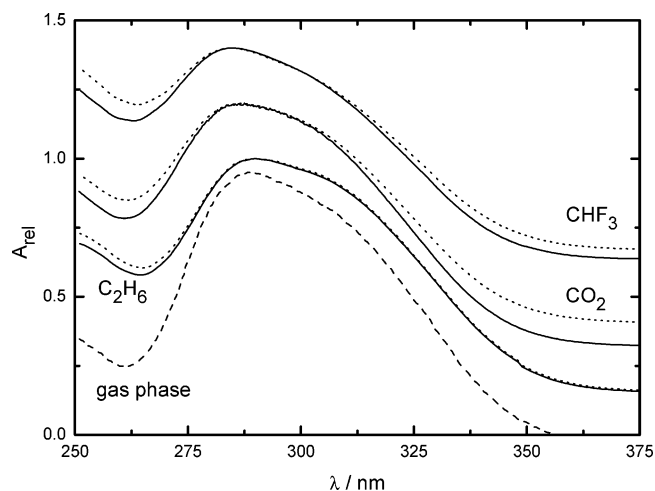


**Figure 1.** First UV-absorption band of  $\text{CH}_2\text{I}_2$  at pressures of 20 (full lines) and 80 MPa (dotted lines) in sc  $\text{CHF}_3$ ,  $\text{CO}_2$ , and  $\text{C}_2\text{H}_6$  (from top to bottom) and in the gas phase under  $\text{CH}_2\text{I}_2$  vapor pressure at ambient temperature (dashed line). Spectra are normalized to peak height and baseline shifted for different solvents.

$\text{CO}_2$ – $\text{CO}_2$ : Two-center Lennard-Jones plus point–quadrupole interaction<sup>55</sup>

$\text{CH}_2\text{I}_2$ – $\text{CH}_2\text{I}_2$ : Lennard-Jones plus point–dipole interaction<sup>56</sup>

$\text{CH}_2\text{I}_2$ – $\text{CO}_2$ : Standard Lorentz–Berthelot mixing rules were applied to obtain the Lennard-Jones part of the solute–solvent potential.

The dipole–quadrupole interaction was implemented by assigning partial charges as follows ( $e$ , elementary charge):

$\text{CH}_2\text{I}_2$ :  $|q| = 0.97314e$ ;  $+q$  on the C atom;  $-q$  on the center of mass (= Lennard-Jones center), distance, 1.0484 Å.

$\text{CO}_2$ :  $|q| = 0.0135e$ ; three partial charges in linear arrangement 1.2088 Å apart,  $-q$  at the two Lennard-Jones centers,  $+2q$  at the C atom.

### 4. Results

The first absorption band of diiodomethane with a maximum close to 290 nm is known to show very little solvent shift between gas phase and liquid solution,<sup>37,57</sup> an observation that also holds for the pressure dependence in sc fluid solution as illustrated in Figure 1. As we reported recently,<sup>24</sup> excitation into this band gives transient absorbance traces quite similar to those observed in liquid solution.<sup>26–28</sup> Figure 2 shows two examples measured in sc  $\text{C}_2\text{H}_6$  at 25 and 75 MPa pressure: the curves consist of a sharp subpicosecond peak followed by an  $\sim 5$ –15 ps exponential rise to an intermediate plateau which subsequently decays on a nanosecond time scale (not visible on the time scale displayed in Figure 2).

As discussed in detail before,<sup>24,28,30</sup> the subpicosecond peak in the probe wavelength range 360–440 nm may be largely attributed to absorption from the Franck–Condon region of the electronically excited state of the parent molecule  $\text{CH}_2\text{I}_2$ . Its rise time is determined by the cross correlation between pump and probe pulses, the fall time is a convolution of the probe pulse and decay of Franck–Condon absorption. A quantitative analysis of the peak signal, however, is complicated by contributions from solvent Kerr effects and the nonlinear electronic response of the window material used in our high-pressure cell which affect the amplitude and rising part of the peak depending on the relative position of the pump and probe beam focus as well as on the strength of focusing. In a careful reexamination of the pressure dependence of the subpicosecond decay including deconvolution with the pump–probe cross correlation, we obtained, in contrast to our earlier report,<sup>24</sup> a



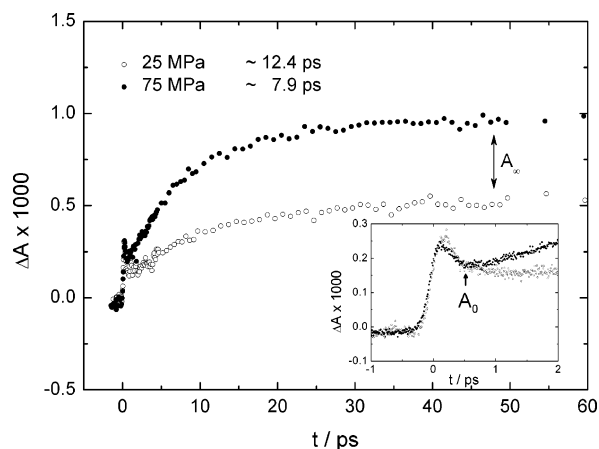


**Figure 2.** Pressure dependence of transient absorbance signal at 405 nm following excitation of  $\text{CH}_2\text{I}_2$  at 305 nm. The solvent is sc  $\text{C}_2\text{H}_6$  at 310 K and pressures of 25 and 75 MPa. Data points are averaged over 500 pump pulses and 6 consecutive time scans. The rise times given in the legend are based on a convolution and fitting procedure including a Gaussian pump–probe cross correlation and two exponential terms to represent the fast decay and the picosecond rise, respectively. The inset shows the initial part of the same signals.

pressure-independent time constant of  $220 \pm 30$  fs at probe wavelengths between 360 and 440 nm. In acetonitrile solution, Tarnovsky et al. give an average decay time of 350 fs (310 nm pump wavelength),<sup>28</sup> Saitow et al. obtained 0.5 ps (268 nm pump/ 400 nm probe),<sup>27</sup> while Schwartz et al. measured 350 fs (310 nm pump/ 610 nm probe) in  $\text{CCl}_4$  and  $\text{CH}_2\text{Cl}_2$  solutions. Considering the widely varying conditions, from polar to nonpolar liquid to nonpolar sc fluid between 100 and 1000 bar pressure, these comparatively small variations between 220 and

350 fs at 305–310 nm excitation wavelength suggest a minor influence of solvent friction and polarity on wave packet motion in the excited state.

The nanosecond decay is barely visible in our measurements and as such not amenable to a quantitative investigation in the experiments discussed here. We will neglect it in the following and refer to a recent study by Tarnovsky et al.<sup>30</sup>

The traces in Figure 2 illustrate the main effects of raising the sc fluid density on which we will concentrate.<sup>24</sup> Most obvious are the increase of the plateau amplitude  $A_\infty$  seen at long delay times at around 200 ps and the decrease of the exponential rise time  $\tau_{\text{rise}}$ . It is evident from the example curves that the “slow” absorption rise does not extrapolate back to zero at early times but to an initial absorbance  $A_0$  which turned out to be less sensitive to the increase of pressure than  $A_\infty$ .<sup>24</sup> Figure 3 shows a sample set of fitted decay curves obtained in compressed sc  $\text{CO}_2$ .

From similar absorbance traces recorded at probe wavelengths between 355 and 435 nm, transient spectra in sc  $\text{CO}_2$ ,  $\text{CHF}_3$ , and  $\text{C}_2\text{H}_6$  have been reconstructed (Figure 4, left column). They reflect the rise in isomer population (intensity increase of the main band around 370 nm) with time and show some indication of spectral narrowing, which is attributed to vibrational cooling of the hot isomer.<sup>24,28</sup> Assuming that the isomer is the species predominantly responsible for absorption in this spectral region and that the oscillator strength associated with the corresponding electronic transition does not change with vibrational excitation, the integrated band intensity is directly proportional to the concentration of isomer. Conversely, if we normalize the measured transient spectra to their integrated intensity, they should only show a temporal evolution reflecting spectral narrowing as the typical signature of vibrational cooling (Figure

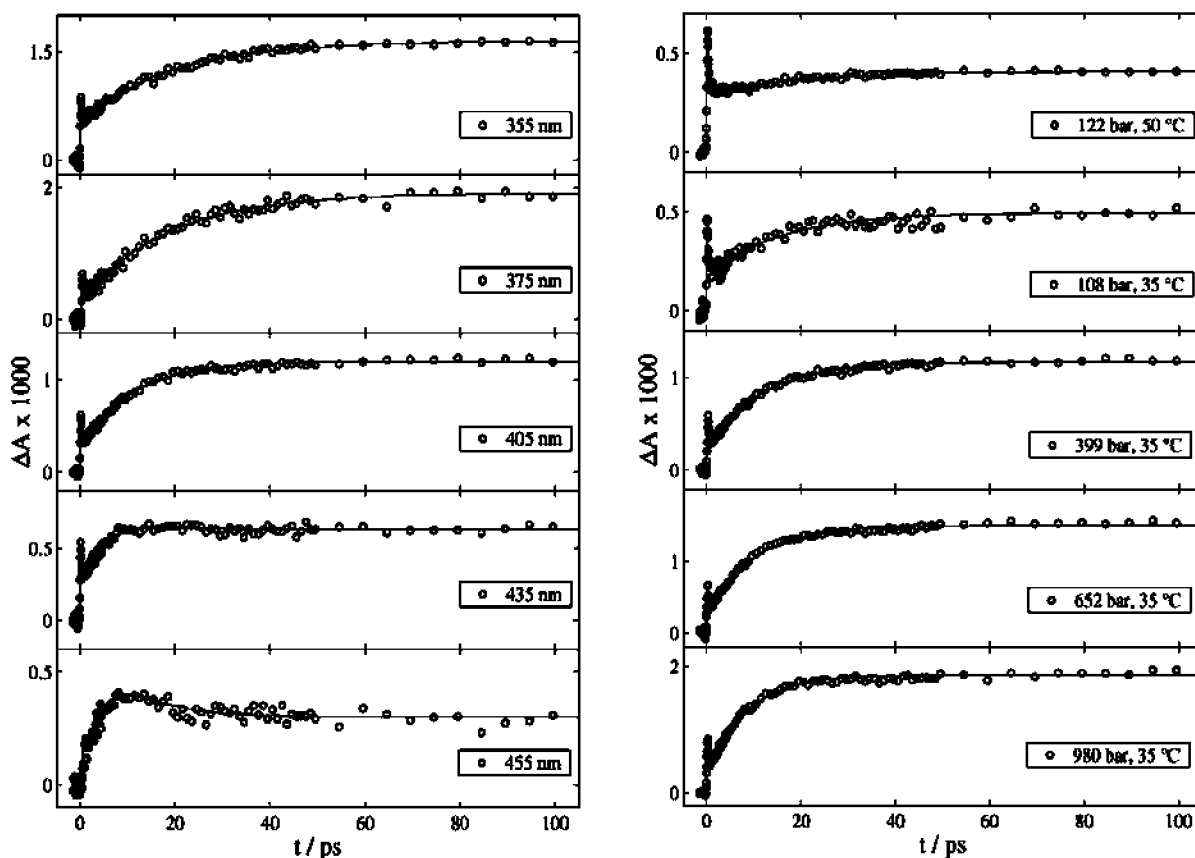


**Figure 3.** Transient absorbance obtained at 305 nm pump wavelength in  $\text{CO}_2$ . Probe wavelength series at constant pressure (40 MPa, left) and pressure series at 405 nm probe wavelength.

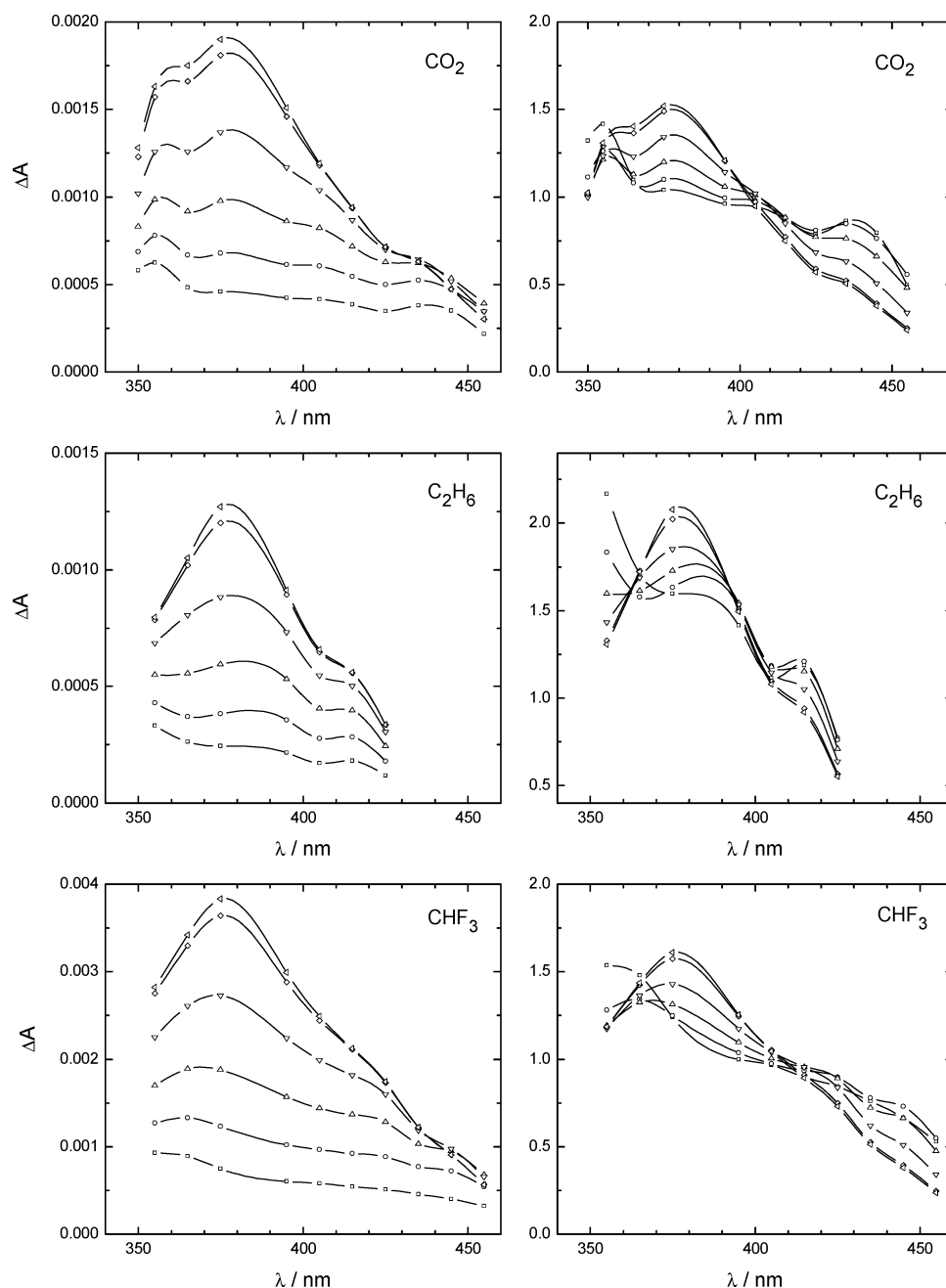


**Figure 4.** Left column: reconstructed transient absorption band at  $\sim 370$  nm measured following 405 nm excitation of  $\text{CH}_2\text{I}_2$  in sc solution at 2 (square), 5 (circle), 10 (up triangle), 20 (down triangle), 50 (diamond), and 100 ps (left-facing triangle) time delay. From top to bottom: sc  $\text{CO}_2$  at 308 K and 40 MPa,  $\text{C}_2\text{H}_6$  at 310 K and 40 MPa, and  $\text{CHF}_3$  at 311 K and 51 MPa. Right column: corresponding normalized spectra (for details, see text).

4, right column). In particular, they allow us to identify a wavelength region between 400 and 410 nm with very little spectral change, in which one may observe isomer formation kinetics practically free of contributions from vibrational relaxation. We checked the underlying assumption by comparing the exponential rise times measured around 405 nm with the rise time of the corresponding integrated absorption band at selected pressures in all three sc solvents. The latter turned out to be consistently 10% smaller than the single wavelength values. Since we focus exclusively on the pressure dependence of amplitudes and rise times, this constant scaling factor does not have any impact on the further discussion. It largely reflects the fact that strictly speaking in spectral narrowing due to vibrational cooling there is no point in the affected absorption band for which the extinction coefficient is totally independent of vibrational temperature. On the other hand, because of

spectral dynamics due to vibrational cooling, rise times measured across the absorption band become longer at probe wavelengths below 405 nm and shorter above. The approximate time scale of vibrational relaxation may be estimated from the decay and rise of the normalized spectra at different wavelengths (Figure 5). A quantitative determination of the vibrational relaxation time  $\tau_{\text{VET}}$  would require knowledge of the dependence of the isomer's extinction coefficient on internal energy or at least temperature, which is not available. However, the observed decay times in the wing of the band are comparable to the value of  $\tau_{\text{VET}}$  measured for  $\text{CH}_2\text{I}_2$  in sc  $\text{CO}_2$  by Sekiguchi et al. at comparable densities.<sup>58</sup>

The assumption that the transient absorption band observed after about 30 ps may be attributed to a single photoproduct is supported by the observation that the shape of the band is independent of fluid density, that is, it is irrelevant which probe

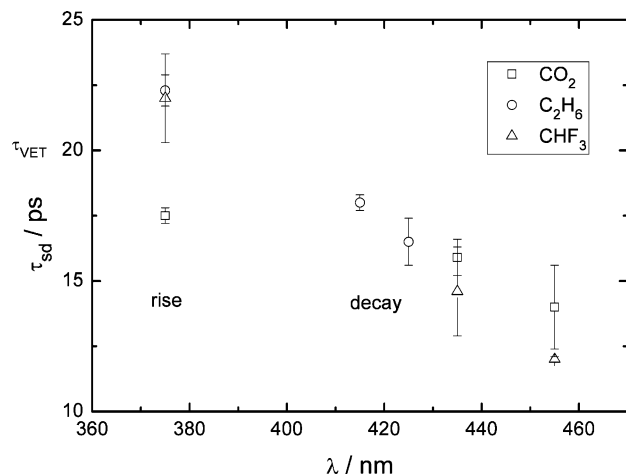


**Figure 5.** Probe wavelength dependence of exponential rise/decay time  $\tau_{sd}$  obtained from an analysis of the normalized transient spectra in Figure 4.  $\tau_{VET}$  indicates the vibrational relaxation time of  $\text{CH}_2\text{I}_2$  in sc  $\text{CO}_2$  from the data given by Sekiguchi et al.<sup>58</sup>

wavelength we chose to evaluate  $A_\infty$  to determine the density dependence of the isomer yield.<sup>24</sup>

In Table 1, we list the exponential picosecond rise times obtained from a convolution and fitting procedure involving a Gaussian pump–probe cross correlation, a fast exponential decay, and the picosecond rise to our transient absorbance signals in sc fluids  $\text{CO}_2$ ,  $\text{CHF}_3$ , and  $\text{C}_2\text{H}_6$ , for a 304/308 nm pump and 405/370 nm probe. At these wavelengths, the inclusion of only a single term for the picosecond rise proved to be entirely adequate, as the addition of a second term improved the quality of fit only marginally. This may seem surprising as the absorbance changes due to isomer formation and vibrational cooling in the same spectral region, but at 405 nm probe wavelength, we have practically no spectral influence of cooling.

At the 370 nm probe, the spectral amplitude of the cooling dynamics is smaller than that of the population rise, and furthermore, the time constants of both components are on the same order of magnitude, which makes it impossible to separate them consistently at sc fluid densities significantly smaller than liquid density. A graphical summary of the rise time data is given in Figure 6, which illustrates the pressure dependence of the corresponding rate coefficients  $\tau_{\text{rise}}^{-1}$  in a log–log representation. Apparently, there is only little variation in the behavior of the rate coefficient between different sc solvents  $\text{CO}_2$ ,  $\text{C}_2\text{H}_6$ , and  $\text{CHF}_3$ . In contrast, one observes a pronounced dependence on probe wavelength which is caused by the spectral narrowing already mentioned. The shape of the pressure dependence, however, does not change, indicating that the process involved in isomer formation might be closely related to vibrational energy relaxation, as has been suggested before.<sup>24,25,28–31</sup>

Both  $\tau_{\text{rise}}^{-1}$  and  $A_\infty$  increase nonlinearly with sc fluid density, an observation that we will discuss in the next section. It should be noted that absolute  $A_\infty$  values in different fluids may not be compared directly, as they strongly depend on excitation conditions and initial parent molecule concentration which were impossible to maintain when switching between fluids.

While the measurements discussed so far were performed with a pump wavelength of  $305 \pm 3$  nm, we also looked at the effect of the excitation energy on rise times and amplitudes (Table 2). At a shorter pump wavelength,  $\tau_{\text{rise}}$  increases, while its density dependence becomes more pronounced.

**TABLE 1: Pressure Dependence of Transient Absorbance Rise Time  $\tau_{\text{rise}}$  in sc Solution at 405/410 and 370 nm Probe Wavelengths after 302–308 nm Excitation**

|  | $p/\text{MPa}$ | $\rho^{59}/\text{mol dm}^{-3}$ | $\tau_{\text{rise}}/\text{ps}$      | $p/\text{MPa}$ | $\rho^{59}/\text{mol dm}^{-3}$ | $\tau_{\text{rise}}/\text{ps}$ |
|--|----------------|--------------------------------|-------------------------------------|----------------|--------------------------------|--------------------------------|
|  | 405 nm probe   |                                |                                     | 370 nm probe   |                                |                                |
| CO <sub>2</sub> 323 K                            | 10.4           | 9.8                            | $20.0 \pm 1.3$                      | 9.4            | 7.3                            | $51.5 \pm 6.0$                 |
|  | 10.7           | 10.7                           | $18.6 \pm 1.2$                      | 9.8            | 8.2                            | $41.2 \pm 3.1$                 |
|  | 11.1           | 11.7                           | $16.8 \pm 3.5$                      | 10.2           | 9.3                            | $43.6 \pm 3.2$                 |
|  | 11.4           | 12.3                           | $23.6 \pm 0.8$                      | 10.5           | 10.1                           | $45.8 \pm 2.6$                 |
|  | 11.8           | 13.0                           | $18.6 \pm 3.1$                      | 10.9           | 11.2                           | $35.1 \pm 1.6$                 |
|  | 12.2           | 13.6                           | $20.4 \pm 3.5$                      | 11.7           | 12.8                           | $37.7 \pm 1.1$                 |
|  | 12.6           | 14.0                           | $20.4 \pm 1.4$                      | 12.4           | 13.8                           | $32.6 \pm 1.0$                 |
|  | 14.2           | 15.4                           | $15.7 \pm 1.4$                      | 13.5           | 14.9                           | $30.6 \pm 1.0$                 |
|  |                |                                |                                     | 15.0           | 15.9                           | $35.7 \pm 1.0$                 |
|  |                |                                |                                     | 18.0           | 17.2                           | $26.9 \pm 1.0$                 |
|  |                |                                |                                     | 21.1           | 18.1                           | $24.7 \pm 0.4$                 |
|  |                |                                |                                     | 42.0           | 21.2                           | $21.7 \pm 1.0$                 |
|  |                |                                |                                     | 54.0           | 22.2                           | $18.4 \pm 1.0$                 |
|  |                |                                |                                     | 69.0           | 23.1                           | $17.6 \pm 1.0$                 |
| CO <sub>2</sub> 308 K                            |                |                                |                                     | 79.0           | 23.7                           | $16.2 \pm 1.0$                 |
|  |                |                                |                                     | 90.0           | 24.2                           | $14.4 \pm 1.0$                 |
|  | 10.8           | 16.8                           | $15.9 \pm 1.0$                      | 11.7           | 17.2                           | $28.9 \pm 0.9$                 |
|  | 16.2           | 18.8                           | $14.8 \pm 0.4$                      | 12.0           | 17.4                           | $29.3 \pm 1.2$                 |
|  | 16.5           | 18.9                           | $13.5 \pm 0.9$                      | 15.0           | 18.5                           | $27.2 \pm 0.6$                 |
|  | 18.0           | 19.3                           | $14.2 \pm 0.4$                      | 17.9           | 19.3                           | $23.1 \pm 1.0$                 |
|  | 20.8           | 19.9                           | $13.9 \pm 0.4$                      | 19.5           | 19.6                           | $28.1 \pm 0.7$                 |
|  | 25.8           | 20.6                           | $13.6 \pm 0.4$                      | 21.1           | 19.9                           | $25.3 \pm 0.3$                 |
|  | 27.0           | 20.8                           | $13.2 \pm 0.7$                      | 25.4           | 20.6                           | $23.7 \pm 0.2$                 |
|  | 31.0           | 21.2                           | $12.4 \pm 0.3$                      | 31.2           | 21.2                           | $22.6 \pm 0.2$                 |
|  | 34.9           | 21.6                           | $11.5 \pm 0.6$                      | 34.5           | 21.6                           | $21.3 \pm 0.3$                 |
|  | 35.8           | 21.7                           | $11.8 \pm 0.3$                      | 35.8           | 21.7                           | $21.5 \pm 0.2$                 |
|  | 39.9           | 22.1                           | $11.3 \pm 0.2$                      | 38.0           | 21.9                           | $21.6 \pm 0.2$                 |
|  | 45.4           | 22.5                           | $10.9 \pm 0.2$                      | 38.2           | 21.9                           | $20.3 \pm 0.2$                 |
|  | 50.0           | 22.8                           | $10.7 \pm 0.2$                      | 38.5           | 21.9                           | $22.0 \pm 0.3$                 |
|  | 51.5           | 22.9                           | $9.9 \pm 0.4$                       | 46.0           | 22.5                           | $20.0 \pm 0.2$                 |
|  | 54.6           | 23.1                           | $10.1 \pm 0.2$                      | 51.5           | 22.9                           | $19.2 \pm 0.2$                 |
|  | 60.0           | 23.5                           | $9.9 \pm 0.3$                       | 56.5           | 23.3                           | $18.2 \pm 0.2$                 |
|  | 60.0           | 23.5                           | $9.9 \pm 0.2$                       | 60.9           | 23.5                           | $17.3 \pm 0.2$                 |
|  | 65.2           | 23.8                           | $9.8 \pm 0.2$                       | 70.0           | 24.0                           | $15.9 \pm 0.2$                 |
| 74.5   | 24.2           | $9.0 \pm 0.2$                  | 75.0                                | 24.3           | $15.0 \pm 0.2$                 |                                |
| 80.5   | 24.5           | $8.5 \pm 0.2$                  | 81.0                                | 24.5           | $14.6 \pm 0.2$                 |                                |
| 85.5   | 24.7           | $9.0 \pm 0.2$                  | 85.0                                | 24.7           | $14.1 \pm 0.2$                 |                                |
| 98.0   | 25.2           | $8.3 \pm 0.2$                  |                                     |                |                                |                                |
| C <sub>2</sub> H <sub>6</sub> 310 K 405 nm probe |                |                                | CHF <sub>3</sub> 308 K 410 nm probe |                |                                |                                |
| 25.0   | 14.0           | $14.3 \pm 0.7$                 | 17.5                                | 14.4           | $15.7 \pm 0.4$                 |                                |
| 45.0   | 15.3           | $12.0 \pm 0.6$                 | 20.0                                | 14.8           | $15.4 \pm 0.4$                 |                                |
| 55.0   | 15.7           | $10.4 \pm 0.4$                 | 30.0                                | 15.9           | $13.4 \pm 0.3$                 |                                |
| 65.0   | 16.1           | $9.7 \pm 0.3$                  | 45.0                                | 16.9           | $11.8 \pm 0.4$                 |                                |
| 75.0   | 16.4           | $8.9 \pm 0.2$                  | 60.0                                | 17.7           | $10.7 \pm 0.3$                 |                                |
| 85.0   | 16.6           | $7.5 \pm 0.2$                  | 80.0                                | 18.5           | $10.4 \pm 0.3$                 |                                |
| 95.0   | 16.8           | $7.8 \pm 0.2$                  | 90.0                                | 18.8           | $8.9 \pm 0.2$                  |                                |

## 5. Discussion

We first will discuss the density dependence of the isomer yield as reflected in  $A_\infty(\rho)$ . As has been suggested,<sup>24,28,30</sup> a solvent cage is a necessary prerequisite for the isomer to be formed, and the “tighter” it becomes the larger the isomer yield will become. It is to be expected, however, that the properties of the solvent cage will be determined by the local sc solvent density  $\rho_{\text{local}}$  in the vicinity of the solute rather than the bulk density  $\rho$  of the solvent. We will estimate the local density on the basis of radial distribution functions  $g(r)$  obtained from classical MD simulations, using the relation  $\rho_{\text{local}} = g_{\text{max}}(\rho, T)\rho$ . As the widest density range was covered in sc  $\text{CO}_2$ , we will restrict our yield analysis to this solvent. Figure 7 shows the dependence of  $g_{\text{max}}$  on bulk density in this solvent at the two temperatures  $T = 308$  and  $323$  K for solute–solvent centers of mass. The stronger enhancement toward low densities is a signature of attractive van der Waals forces that become increasingly important toward lower density. The temperature

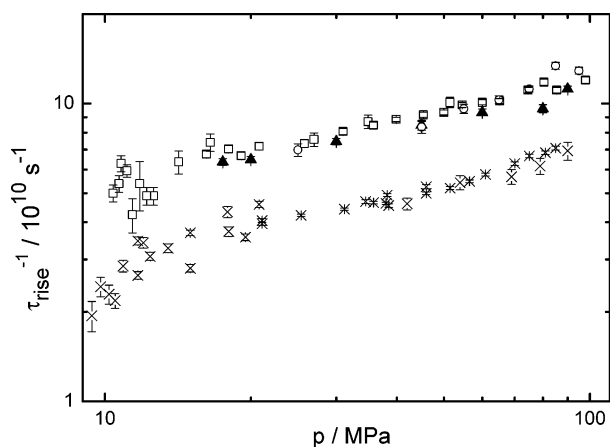


**Figure 6.** Pressure dependence of the inverse absorbance rise times listed in Table 1. ( $\square$ ), sc  $\text{CO}_2$  405 nm probe; ( $\times$ ), sc  $\text{CO}_2$  370 nm probe; ( $\blacktriangle$ ), sc  $\text{CHF}_3$  410 nm probe; ( $\circ$ ), sc  $\text{C}_2\text{H}_6$  405 nm probe.

**TABLE 2: Rise Time  $\tau_{\text{rise}}$  of Transient Absorbance at 405 nm, Pressure Dependence in sc  $\text{CO}_2$  at 308 K<sup>a</sup>**

| $p/\text{MPa}$ | $\rho/\text{mol dm}^{-3}$ | $\tau_{\text{rise}}/\text{ps}$ |
|----------------|---------------------------|--------------------------------|
| 263 nm         |                           |                                |
| 45.7           | 22.5 <sup>b</sup>         | $24.1 \pm 0.9$                 |
| 82.5           | 24.6 <sup>b</sup>         | $18.2 \pm 0.6$                 |
| 276 nm         |                           |                                |
| 28.5           | 20.9                      | $25.3 \pm 0.8$                 |
| 37.5           | 21.9                      | $22.9 \pm 0.6$                 |
| 39.0           | 22.0                      | $21.6 \pm 0.7$                 |
| 49.5           | 22.8                      | $20.0 \pm 0.5$                 |
| 58.6           | 23.4                      | $17.2 \pm 0.4$                 |
| 69.0           | 24.0                      | $16.5 \pm 0.4$                 |
| 87.3           | 24.8                      | $13.6 \pm 0.2$                 |
| 350 nm         |                           |                                |
| 19.0           | 19.5                      | $7.8 \pm 0.3$                  |
| 24.6           | 20.4                      | $7.6 \pm 0.3$                  |
| 30.2           | 21.1                      | $7.3 \pm 0.2$                  |
| 31.5           | 21.3                      | $6.6 \pm 0.3$                  |
| 35.7           | 21.7                      | $6.9 \pm 0.2$                  |
| 40.0           | 22.1                      | $6.5 \pm 0.3$                  |
| 40.4           | 22.1                      | $6.7 \pm 0.2$                  |
| 45.1           | 22.5                      | $6.9 \pm 0.2$                  |
| 50.4           | 22.9                      | $6.9 \pm 0.2$                  |
| 55.0           | 23.2                      | $6.5 \pm 0.3$                  |
| 55.6           | 23.2                      | $6.7 \pm 0.2$                  |
| 60.3           | 23.5                      | $6.5 \pm 0.1$                  |
| 65.2           | 23.8                      | $6.5 \pm 0.1$                  |
| 70.3           | 24.0                      | $6.1 \pm 0.1$                  |
| 76.0           | 24.3                      | $6.1 \pm 0.2$                  |
| 79.9           | 24.5                      | $6.1 \pm 0.1$                  |
| 87.0           | 24.8                      | $5.4 \pm 0.2$                  |
| 87.7           | 24.8                      | $5.8 \pm 0.1$                  |
| 95.7           | 25.1                      | $5.7 \pm 0.1$                  |

<sup>a</sup> Excitation wavelengths 263, 276, and 350 nm. <sup>b</sup> Reference 59.

dependence is fairly weak as expected for a 5% change, so we use a common polynomial interpolation to calculate  $\rho_{\text{local}}$ .

Figure 8 shows a plot of  $A_\infty$  and  $A_0$  vs  $\rho_{\text{local}}$  as calculated by eq 1. We show the absorbance amplitudes measured at a probe wavelength of 370 nm, because of the significantly better signal-to-noise ratio in particular at low densities as compared to the amplitude data obtained at 405 nm. The amplitudes  $A_\infty$  and  $A_0$  are baseline corrected and normalized to absorbed pump energy as gauged by the height of the initial Franck–Condon absorption peak, which shows a linear increase with solvent density caused by increasing solubility of diiodomethane in the sc solvent.  $A_0$  values were obtained from back-extrapolation of the deconvoluted kinetics, using the pump–probe cross correlation width

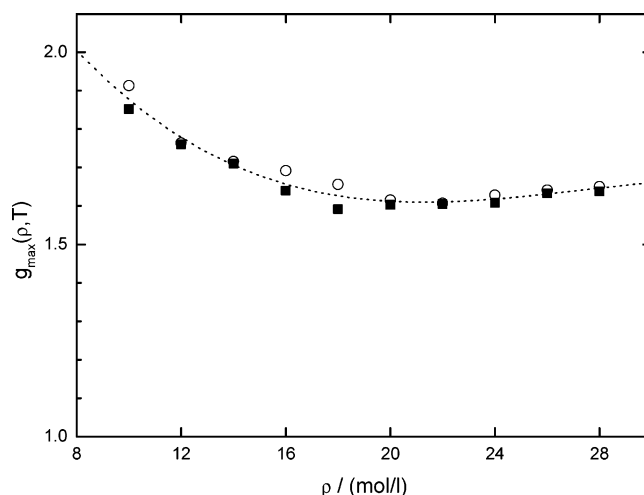


**Figure 7.** Maximum values of the  $\text{CH}_2\text{I}_2$ – $\text{CO}_2$  center-of-mass radial distribution function vs the bulk density  $\rho$  of sc  $\text{CO}_2$ :  $T = 308 \text{ K}$  ( $\circ$ ) and  $T = 323 \text{ K}$  ( $\blacksquare$ ). The dotted line represents the numerical interpolation used for calculating local densities.

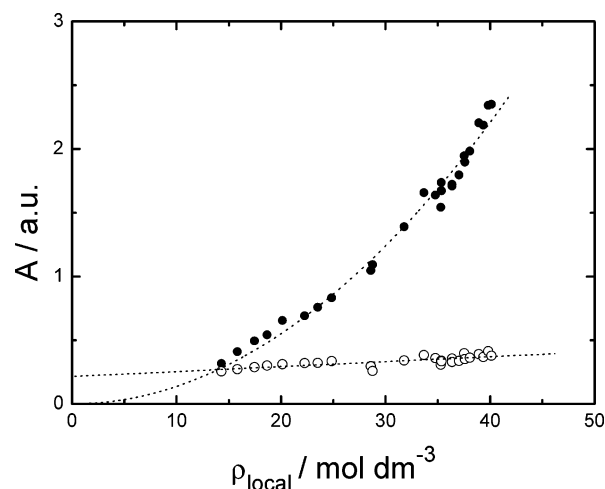


**Figure 8.** Normalized amplitudes at 370 nm probe wavelength vs local density of sc  $\text{CO}_2$  in the vicinity of the  $\text{CH}_2\text{I}_2$  solute:  $A_\infty$  ( $\bullet$ ) and  $A_0$  ( $\circ$ ). The dotted lines illustrate quadratic and linear dependence.

at the corresponding density. (We observed virtually no effect of sc fluid density on cross correlation width throughout the pressure range studied.)

We find a quadratic dependence of  $A_\infty$  on local density and a fairly weak, approximately linear dependence of  $A_0$ . In analogy to the observed density dependence of the photodissociation quantum yield of iodine, which to good approximation is linear in solvent density for quantum yields  $0.9 \geq \Phi_d \geq 0.1$ ,<sup>21,22</sup> we suggest that this quadratic dependence of  $A_\infty$  may be taken as evidence for an isomer formation mechanism that involves two consecutive stages at each of which escape from the solvent cage may occur. The quantum yield at each of these would linearly depend on density.

In Figure 9, we show a simple mechanism that would be consistent with this suggestion and give an overall isomer quantum yield  $\Phi_{\text{iso}} = \Phi_1 \Phi_2 \propto \rho_{\text{local}}^2$ . It rests on the assumption that in the probe wavelength region from 360 to 440 nm only the isomer contributes to  $A_\infty$ , while  $A_0$  is due to absorption by the rapidly formed loosely bound complex between the iodine atom and the vibrationally highly excited methyl iodide radical in the solvent cage, hence,  $A_0 \sim \Phi_1$  and  $A_\infty \sim \Phi_1 \Phi_2$ . The intermediate complex may be stabilized by charge transfer (CT) interactions between the atom and radical or dipole–induced–

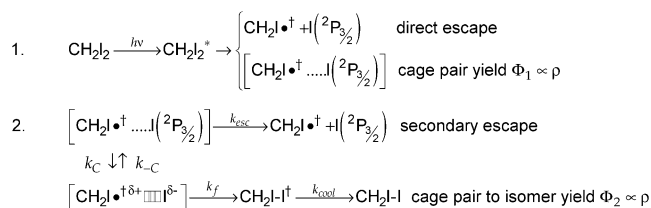


**Figure 9.** Kinetic model of isomer formation. The large dot denotes the radical, the dagger indicates vibrational excitation, and the asterisk denotes electronic excitation.  $\delta^+$  and  $\delta^-$  indicate a weak interaction between the dipolar radical and the highly polarizable iodine atom that leads to a weakly bound complex, indicated by the big dots.

dipole interaction. In both cases, one might expect a sufficiently strong absorption causing the initial  $A_0$  signal. If one introduces a further simplification by assuming that equilibration between the cage pair and the complex is sufficiently rapid compared to  $k_{\text{esc}}$  and  $k_{\text{f}}$ , such that  $k_{\text{C}}/k_{-\text{C}} \approx K_{\text{C}}$ , one obtains expressions for the yields  $\Phi_2$  and the formation rate constant  $k_{\text{iso}}$  of the “hot” isomer

$$\begin{aligned}
 \Phi_2 &\approx \frac{K_{\text{C}}k_{\text{f}}}{K_{\text{C}}k_{\text{f}} + k_{\text{esc}}} \\
 \text{and} \\
 k_{\text{iso}} &\approx K_{\text{C}}k_{\text{f}} + k_{\text{esc}}
 \end{aligned}$$

We are aware that this is an oversimplified scheme designed to rationalize the variation of the observable kinetic parameters with density. In particular, it does not explicitly take into account  $k_{\text{C}}$ ,  $k_{-\text{C}}$ , and the concurrent vibrational cooling of the hot radical which would be dynamically coupled, nor do we include a route of in-cage recombination to the parent molecule. The latter, however, has not been observed<sup>24,25,28,30</sup> and is not expected to be efficient, as the orientation correlation between the radical and the iodine atom is rapidly lost. In the discussion here, we also do not further consider the fact that 304 nm excitation populates two excited electronic states<sup>36</sup> leading to an appreciable fraction of excited iodine atoms ( $\text{I}({}^2\text{P}_{1/2})$ , briefly  $\text{I}^*$ )<sup>38–40</sup> and ground-state iodine atoms ( $\text{I}({}^2\text{P}_{3/2})$ , briefly  $\text{I}$ ) in two different populations.<sup>41</sup> We would like to refer to a recent detailed discussion of the consequences concerning in particular vibrational energy transfer from the hot intermediate radical.<sup>60</sup> The main implication for the present study is that bi- or even trimodal initial vibrational energy distributions that result from the initial population of different electronic states of the parent  $\text{CH}_2\text{I}_2$  make no difference as far as the observable effects of vibrational cooling are concerned. Further, since we monitor the ground-state absorption of the isomer in the wavelength region between 350 and 440 nm, we do not consider the possible contributions from  $\text{I}^*$  processes, as  $\text{I}^*$  only correlates with electronically excited states of the isomer, as we discussed previously.<sup>24</sup>

Within the model, one would expect the amplitude ratio  $A_\infty/A_0 \propto \Phi_2$  to rise linearly with density which we illustrate in Figure 10. Unfortunately, not knowing the ratio of extinction coefficients of the hot complex to that of the isomer, we cannot estimate  $\Phi_2(\rho)$  to carry the analysis further at this stage. From an extrapolation of the linear fit, one may estimate that  $\Phi_2(\rho)$  approaches zero at a local solvent density of about  $9.1 \text{ mol dm}^{-3}$ , corresponding to a reduced bulk density of  $\text{CO}_2$ ,  $\rho_{\text{r}} = 0.45$ . Whether this value represents the true onset density for the in-cage isomerization channel remains to be clarified in further experiments.

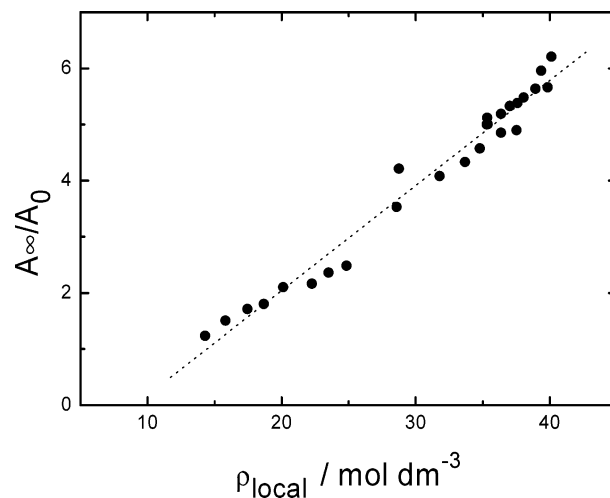


**Figure 10.** Amplitude ratio  $A_\infty/A_0$  at 370 nm probe wavelength vs local density of sc  $\text{CO}_2$ . The dotted line represents a linear fit to the data.

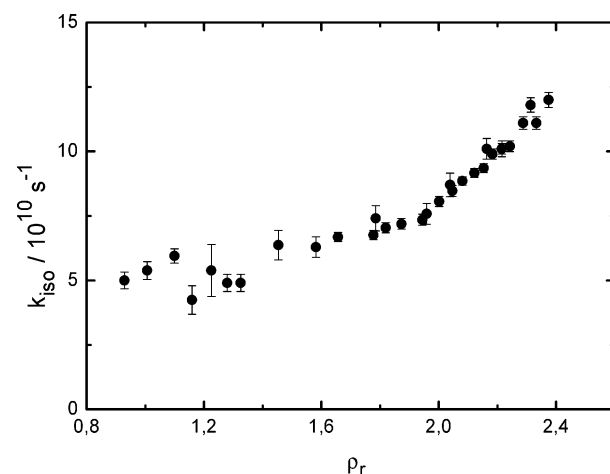


**Figure 11.** Isomer formation rate constant in sc  $\text{CO}_2$  measured at a 405 nm probe wavelength.

We now turn to the density dependence of the rise time  $\tau_{\text{rise}}$ , which directly relates to that of the isomer formation rate,  $k_{\text{iso}} \approx \tau_{\text{rise}}^{-1}$  (405 nm).<sup>24,25</sup> If we assume that collisional stabilization plays a crucial role in isomer formation<sup>24,28</sup> and that the change of collision rate controlled  $k_{\text{f}}$  makes the dominant contribution to the observed  $k_{\text{iso}}(\rho)$  dependence, then one would expect  $k_{\text{iso}}$  to depend linearly on the collision rate in sc solution, if higher frequency solute modes ( $> 200 \text{ cm}^{-1}$ ) were mainly involved in vibrational cooling of the complexed radical.<sup>61</sup> Such a linear dependence is not observed in our experiments (Figure 11).

Alternatively, if one assumes that transfer of the vibrational excess energy to the solvent occurs mainly via low-frequency modes, one might adopt an empirical approach and use the mass-weighted zero frequency friction coefficient  $\xi$  as a measure for the collision rate.<sup>62,63</sup> In this approximation, it may be useful to consider the pressure-dependent bulk viscosity  $\eta(\rho)$  of the solvent as a means to estimate the collision rate, mass-scaling it with respect to  $\text{CO}_2$ . Figure 12 shows the resulting plot of  $k_{\text{iso}}$  vs  $\eta$ . The observed linear dependence supports the hypothesis that  $k_{\text{iso}}$  to a large extent is controlled by collisional stabilization of the vibrationally hot intermediate via low-frequency modes. The viscosity-independent offset between  $k_{\text{iso}}$  in different solvents could be due to static interactions that influence the stability of the intermediate complex via  $K_{\text{C}}$ , but



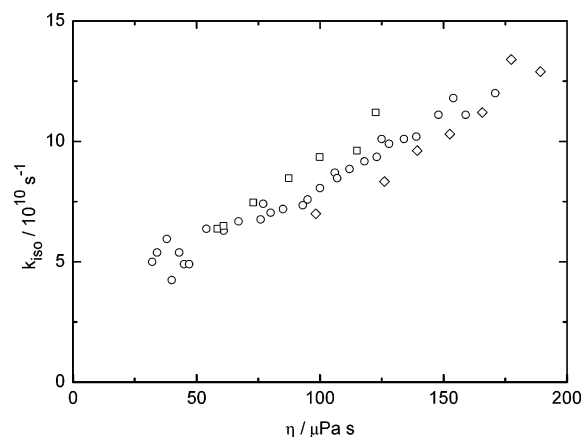


**Figure 12.** Isomer formation rate coefficients  $k_{\text{iso}}$  vs viscosity<sup>59</sup> in sc solvents  $\text{CO}_2$  ( $\circ$ ),  $\text{C}_2\text{H}_6$  ( $\square$ ), and  $\text{CHF}_3$  ( $\diamond$ ). Viscosities were taken from ref 59 and scaled by factors of 1.47 and 0.63 for ethane and fluoroform, respectively, to correct for solvent molar mass with respect to  $\text{CO}_2$ .

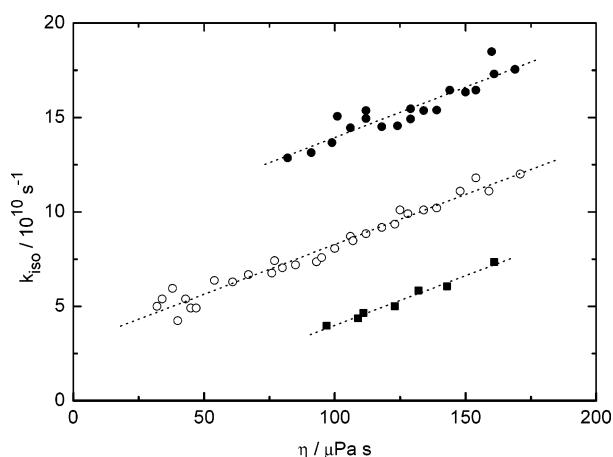


**Figure 13.** Viscosity dependence of isomer formation rate coefficients  $k_{\text{iso}}$  vs viscosity in sc solvents  $\text{CO}_2$  at different excitation wavelengths: ( $\circ$ ), 405 nm; ( $\bullet$ ), 350 nm; ( $\blacksquare$ ), 272 nm.

the main role of the solvent seems to be restricted to that of a dissipative bath.

A linear correlation between  $k_{\text{iso}}$  and  $\eta$  in sc  $\text{CO}_2$  also holds for the other excitation wavelengths as shown in Figure 13. The rate coefficients just change by a constant factor as the excitation energy is varied. It should be stressed again that this change cannot be caused by different dissociation channels of the parent molecule that open up as the pump wavelength is varied: direct in-cage recombination to the electronic ground state of the diiodomethane isomer—which is the process we are observing—can only occur between a  $\text{CH}_2\text{I}$  radical and an  $\text{I}(\text{P}_{3/2})$  atom. Spin-orbit relaxation of the excited iodine atom may be excluded on our time scale. In terms of our simple model, the observed decrease of  $k_{\text{iso}}$  with increasing internal energy of the radical may be associated with a decrease of  $K_{\text{C}}$ , reflecting the observation that recombination reactions proceeding across low reaction barriers via an intermediate complex often tend to exhibit negative activation energies.<sup>64</sup> This observation lends strong support to our hypothesis of the role of a loosely bound atom–radical complex. We also expect that we would observe a similar effect in a situation where the solvent is very ineffective in taking up the excess vibrational energy from the hot radical, which would be the case in sc xenon. First measurements of a study underway in our laboratory indicate that this is indeed the case.<sup>65</sup>

## 6. Conclusion

We have presented a simple kinetic analysis of diiodomethane isomer formation times and amplitudes following femtosecond photolysis of parent diiodomethane in sc solution at different pressures. The presence of two consecutive competing cage escape processes could be established on the basis of the observed quadratic dependence of overall isomer yield on local sc fluid density. We could confirm the dominant role of collisional stabilization of a highly vibrationally excited intermediate radical–atom complex in the photoinduced isomer formation. The linear dependence of the formation rate constant on sc solvent viscosity seems to suggest a vibrational cooling mechanism that involves low-frequency modes of the solute. We are aware that these conclusions based on a purely kinetic analysis require further investigation. For this purpose, MD simulations of the VER process are underway to look into the dynamics of vibrational energy flow from the radical through low-frequency complex modes into the solvent. Also, quantum-chemical calculations are required to map out relevant parts of the potential energy surface necessary to understand, for example, the excitation energy dependence in more detail.

**Acknowledgment.** The authors thank Dirk Schwarzer for many helpful discussions and Matthias Kling for experimental help in the early stages of this project. Financial support by the Deutsche Forschungsgemeinschaft (SFB 375) is gratefully acknowledged. Above all, the authors would like to express their gratitude to Jürgen Troe for his constant support and encouragement. We have kept enjoying his friendly criticism and stimulating comments that over the years have been essential to bringing this and many other projects along.

## References and Notes

- (1) Franck, J.; Rabinowitsch, E. *Trans. Faraday. Soc.* **1934**, *30*, 120–131.
- (2) Zimmerman, J.; Noyes, R. M. *J. Chem. Phys.* **1950**, *18*, 658.
- (3) Lampe, F. W.; Noyes, R. M. *J. Am. Chem. Soc.* **1954**, *76*, 2140.
- (4) Meadows, L.; Noyes, R. M. *J. Am. Chem. Soc.* **1960**, *82*, 1872.
- (5) Booth, D.; Noyes, R. M. *J. Am. Chem. Soc.* **1960**, *82*, 1868.
- (6) Luther, K.; Troe, J. *Chem. Phys. Lett.* **1974**, *24*, 85–87.
- (7) Otto, B.; Schroeder, J.; Troe, J. *J. Chem. Phys.* **1984**, *81*, 202.
- (8) Nesbitt, D. J.; Hynes, J. T. *J. Chem. Phys.* **1982**, *77*, 2130–2143.
- (9) Chuang, T. J.; Hoffmann, G. W.; Eienthal, K. B. *Chem. Phys. Lett.* **1974**, *25*, 201–205.
- (10) Harris, A. L.; Brown, J. K.; Harris, C. B. *Annu. Rev. Phys. Chem.* **1988**, *39*, 341–366 and references cited therein.
- (11) Lienau, Ch.; Zewail, A. H. *J. Phys. Chem.* **1996**, *100*, 18629.
- (12) Wan, C.; Gupta, M.; Baskin, J. S.; Kim, Z. H.; Zewail, A. H. *J. Chem. Phys.* **1997**, *106*, 4353–4356.
- (13) Bunker, D. L.; Jacobson, B. S. *J. Am. Chem. Soc.* **1972**, *94*, 1843–1848.
- (14) Murrell, J. N.; Stace, A. J.; Dammel, R. *J. Chem. Soc., Faraday Trans. 2* **1978**, *74*, 1532–1539.
- (15) Bergsma, J. P.; Reimers, J. R.; Wilson, K. R.; Hynes, J. T. *J. Chem. Phys.* **1986**, *85*, 5625–5643.
- (16) Brown, J. K.; Harris, C. B.; Tully, J. C. *J. Chem. Phys.* **1988**, *89*, 6687.
- (17) Ben-Nun, M.; Levine, R. D. *J. Phys. Chem.* **1993**, *97*, 2334–2343.
- (18) Ben-Nun, M.; Levine, R. D.; Jonas, D. M.; Fleming, G. R. *Chem. Phys. Lett.* **1995**, *245*, 629–638.
- (19) Wang, W.; Nelson, K. A.; Xiao, L.; Coker, D. F. *J. Chem. Phys.* **1994**, *101*, 9663–9671.
- (20) Batista, V. S.; Coker, D. F. *J. Chem. Phys.* **1996**, *105*, 4033–4054.
- (21) Ooe, H.; Kimura, Y.; Kerazima, M.; Hirota, N. *J. Phys. Chem. A* **1999**, *103*, 7730–7741.
- (22) Schröder, Ch.; Schroeder, J.; Schwarzer, D. *Z. Phys. Chem.* **2001**, *215*, 183–195.
- (23) Denisov, E. T.; Denisova, G.; Polikova, T. S. In *Handbook of Free Radical Initiators*; Denisov, E. T., Ed.; Wiley-Interscience: Hoboken, NJ, 2003; Chapter 2, pp 17–40.
- (24) Grimm, Ch.; Kling, M.; Schroeder, J.; Troe, J.; Zerbs, J. *Isr. J. Chem.* **2003**, *43*, 305–317.

- (25) Grimm, Ch.; Zerbs, J.; Kling, M.; Schroeder, J. In *Femtochemistry and Femtobiology*; Martin, M. M., Hynes, J. T., Eds.; Elsevier: Amsterdam, The Netherlands, 2004; pp 257–260.
- (26) Schwartz, B. J.; King, J. C.; Zhang, J. Z.; Harris, C. B. *Chem. Phys. Lett.* **1993**, 203, 503–508.
- (27) Saitow, K.-I.; Naitoh, Y.; Tominaga, K.; Yoshihara, K. *Chem. Phys. Lett.* **1996**, 262, 621–626.
- (28) Tarnovsky, A. N.; Alvarez, J. L.; Yartsev, A. P.; Sundström, V.; Åkesson, E. *Chem. Phys. Lett.* **1999**, 312, 121–130.
- (29) Wall, M.; Tarnovsky, A. N.; Pascher, T.; Sundström, V.; Åkesson, E. *J. Phys. Chem. A* **2003**, 107, 211–217.
- (30) Tarnovsky, A. N.; Sundstrom, V.; Åkesson, E.; Pascher, T. *J. Phys. Chem. A* **2004**, 108, 237–249.
- (31) Odelius, M.; Kadi, M.; Davidsson, J.; Tarnovsky, A. N. *J. Chem. Phys.* **2004**, 121, 2208–2214.
- (32) Zheng, X. M.; Phillips, D. L. *J. Phys. Chem. A* **2000**, 104, 6880–6886.
- (33) Kwok, W. M.; Ma, C. S.; Parker, A. W.; Phillips, D.; Towrie, M.; Matousek, P.; Phillips, D. L. *J. Chem. Phys.* **2000**, 113, 7471–7478.
- (34) Li, Y. L.; Wang, D. Q.; Leung, K. H.; Phillips, D. L. *J. Phys. Chem. A* **2002**, 106, 3463–3468.
- (35) Davidsson, J.; Poulsen, J.; Cammarata, M.; Georgiu, P.; Wouts, R.; Katona, G.; Jacobson, F.; Plech, A.; Wulff, M.; Nyman, G.; Neutze, R. *Phys. Rev. Lett.* **2005**, 94, 245503.
- (36) Kawasaki, M.; Lee, S. J.; Bersohn, R. *J. Chem. Phys.* **1975**, 63, 809–814.
- (37) Baughcum, S. L.; Leone, S. R. *J. Chem. Phys.* **1980**, 72, 6531–6545.
- (38) Koffend, J. B.; Leone, S. R. *Chem. Phys. Lett.* **1981**, 81, 136–141.
- (39) Hunter, T. F.; Kristjansson, K. S. *Chem. Phys. Lett.* **1982**, 90, 35–40.
- (40) Jung, K.-W.; Ahmadi, T. S.; El-Sayed, M. A. *Bull. Korean Chem. Soc.* **1997**, 18, 1274–1280.
- (41) Xu, H. F.; Guo, Y.; Liu, S. L.; Ma, X. X.; Dai, D. X.; Sha, G. H. *J. Chem. Phys.* **2002**, 117, 5722–5729.
- (42) Kisiel, Z.; Pszczolkowski, L.; Caminati, W.; Favero, P. G. *J. Chem. Phys.* **1996**, 105, 1778–1785.
- (43) Zhang, J.; Heller, E. J.; Huber, D.; Imre, D. G.; Tannor, D. *J. Chem. Phys.* **1988**, 89, 3602–3611.
- (44) Barinovs, G.; Markovic, N.; Nyman, G. *J. Chem. Phys.* **1999**, 111, 6705–6711.
- (45) Maier, G.; Reisenauer, H. P.; Hu, J.; Schaad, L. J.; Hess, B. A., Jr. *J. Am. Chem. Soc.* **1990**, 112, 5117–5122.
- (46) Tarnovsky, A. N.; Wall, M.; Rasmusson, M.; Pascher, T.; Åkesson, E. *J. Chin. Chem. Soc.* **2000**, 47, 769–772.
- (47) Tarnovsky, A. N.; Wall, M.; Gustafsson, M.; Lascoux, N.; Sundström, V.; Åkesson, E. *J. Phys. Chem. A* **2002**, 106, 5999–6005.
- (48) Zheng, X. M.; Phillips, D. L. *J. Chem. Phys.* **2000**, 113, 3194–3203.
- (49) Zheng, X. M.; Phillips, D. L. *Chem. Phys. Lett.* **2000**, 324, 175–182.
- (50) Kwok, W. M.; Ma, C. S.; Phillips, D.; Parker, A. W.; Towrie, M.; Matousek, P.; Phillips, D. L. *Chem. Phys. Lett.* **2001**, 341, 292–298.
- (51) Kwok, W. M.; Ma, C.; Parker, A. W.; Phillips, D.; Towrie, M.; Matousek, P.; Zheng, X.; Phillips, D. L. *J. Chem. Phys.* **2001**, 114, 7536–7543.
- (52) Schwarzer, D.; Troe, J.; Votsmeier, M.; Zerezke, M. *J. Chem. Phys.* **1996**, 105, 3121–3131.
- (53) Schwarzer, D.; Troe, J.; Zerezke, M. *J. Chem. Phys.* **1997**, 107, 8380–8390.
- (54) Refson, K. *Comput. Phys. Comm.* **2000**, 126.
- (55) Vrabec, J.; Stoll, J.; Hasse, H. *J. Phys. Chem. B* **2001**, 105, 12126.
- (56) Stoll, J.; Vrabec, J.; Hasse, H. *J. Chem. Phys.* **2003**, 119, 11396.
- (57) Zhang, J.; Imre, D. G. *J. Chem. Phys.* **1988**, 89, 309–313.
- (58) Sekiguchi, K.; Shimojima, A.; Kajimoto, O. *Chem. Phys. Lett.* **2002**, 356, 84–90.
- (59) *NIST Chemistry WebBook*, 69th ed., 2003.
- (60) Lenzer, T.; Oum, K.; Schroeder, J.; Sekiguchi, K. *J. Phys. Chem. A* **2005**, 109, 10824–10831.
- (61) Vikhrenko, V.; Schwarzer, D.; Schroeder, J. *Phys. Chem. Chem. Phys.* **2001**, 3, 1000–1010.
- (62) Zwanzig, R. *J. Chem. Phys.* **1961**, 34, 1931–1935.
- (63) Grote, R. F.; Hynes, J. T. *J. Chem. Phys.* **1982**, 77, 3736–3743.
- (64) Troe, J. *J. Chem. Soc., Faraday Trans.* **1994**, 90, 2303–2317.
- (65) Wagener, P. Diploma thesis, Göttingen, Germany, 2004. Zerbs, J. Ph.D. Thesis, Göttingen, Germany, 2005.